On the effects of large-scale environment and surface types on convective cloud characteristics over Darwin, Australia

Vickal V. Kumar[1,2], Alain Protat[2], Peter T. May[2], Christian Jakob[1], Guillaume Penide[3], Sushil Kumar[4], Laura Davies[1]

[1]School of Mathematical Sciences, Monash University, Australia.

[2]Centre for Australian Weather and Climate Research: A partnership between the Bureau of Meteorology and CSIRO, Melbourne, Australia.

[3]Université Sciences et Technologie de Lille, UFR de Physique Bâtiment P5 Laboratoire d'optique atmosphérique.

[4]School of Engineering and Physics, The University of the South Pacific, Fiji Islands.

Corresponding Author

Vickal V. Kumar

E-mail: v.kumar@bom.gov.au

Address: 25 Arum Walk, Mernda, Victoria, 3754, Australia,

Abstract

Two seasons of Darwin C-band polarimetric (CPOL) research radar, radiosoundings and lightning data are examined to study the relative influence of the large-scale atmospheric regimes and the underlying surface types on tropical convective clouds properties and their diurnal evolution. We find that in the 'deep westerly' regime, which corresponds to the monsoon period, the convective cloud occurrence rate is highest consistent with its highest relative humidity. However, these convective clouds have relatively low cloud top heights, smaller than average cell volumes and are electrically least active. In this regime, the cloud cell volume does not vary significantly across different underlying surfaces and afternoon convective activity is suppressed. Thus, the picture emerging is that the convective cloud activity in the deep westerly regime is primarily regulated by the large-scale conditions. The remaining regimes ('easterly', 'shallow westerly' and 'moist easterly') also demonstrate strong dependence on the large-scale forcing and a secondary dependence on the underlying surface type. The 'easterly' regime has a small convective cloud occurrence rate and low cloud heights but the higher lightning counts per convective cloud. The other two regimes have moderate convective cloud occurrence rates and larger cloud sizes. The 'easterly', 'shallow westerly' and 'moist easterly' regimes exhibit a strong, clearly defined semidiurnal convective cloud occurrence pattern, with peaks in the early morning and afternoon periods. The cell onset times in these three regimes depend on the combination of local time and underlying surface.

1. Introduction

Convection patterns in the vicinity of Darwin, a site typical of the monsoon climate of Northern Australia, have been investigated using ground remote sensing observations (e.g. Keenan and Carbone; 1992, Rutledge et al. 1992; Williams et al. 1992; May et al. 2008; Protat et al. 2011). The main reasons for focusing on Darwin are that 1) the site has one of the most comprehensive long-term meteorological observational networks anywhere in the tropics, and 2) it experiences a wide variety of convective systems, and therefore should have important implications for the wider tropical Asia Pacific region. Furthermore, the Darwin site combines seasonally varying meteorological conditions with distinct dry, wet and transition seasons, with a complex topography of coastlines, islands and oceanic areas. This makes Darwin an ideal location to investigate the relative roles of large-scale meteorology and surface types.

Past studies using data around Darwin explored the statistical characteristics of convection, where meteorological regimes were broadly separated into two categories; the build-up/break periods with low-level easterly winds and monsoon periods with low-level westerly winds (e.g. Keenan and Carbone, 1992; Rutledge et al. 1992; Williams et al. 1992; May and Ballinger, 2007). In break periods, cloud cells were reported to be more intense, taller and electrically more active compared to monsoon periods. However, the daily total rain accumulation is higher during monsoon periods, with a ~50 % contribution from stratiform rain (May et al. 2012).

Recent cluster analysis of thermodynamic sounding data using 49 wet seasons (defined as October to April) of radiosonde measurements showed that the Darwin wet season can be subdivided into five objective regimes, which have significantly different synoptic environments (Pope et al. 2009a). These regimes have been shown to be associated with significantly different properties of ice clouds for the Darwin region (Protat et al. 2011). Consequently it is worthwhile to investigate how convective cloud properties may change when data are separated into the five regimes instead of using the simple monsoon / break separation. Such a separation can aid the evaluation and development of convective parameterizations in models (e.g. Jakob, 2003; 2010) as it can help better identify the relationship between the large-scale state (as defined by the cluster regimes) and small-scale cloud properties.

Several convective cloud properties will be considered in this study, including convective cloud occurrence and convective cloud top heights, volume, kinematics, cell onset times and electrical properties. Another important element affecting the growth of convective cloud systems is the merging of individual clouds since this leads to formation of larger cloud systems (Westcott, 1994; Simpson et al. 1993). Previous research efforts in this area generally focused on a single convective cloud property. For example, Westcott (1994) considered case studies of convective cell merging and proposed that merging occurs due to horizontal expansion. Carbone et al. (2000) studied the Hector storms over Tiwi islands and found that they formed mostly due to sea breeze convergence. Pope et al. (2009b), using six wet seasons of satellite observations, found that in the North Australian region, mesoscale convective systems (MCSs) during the westerly (easterly) flow generally first formed over the western (eastern) side of Australia and then move across the continent. Building on these previous studies, a unified study of several convective cloud properties as to be carried out here will provide a more complete understanding of convective cloud properties and competing factors that regulate cloud growth.

May and Ballinger (2007) considered a small subset of aforementioned convective cloud properties for the Darwin region, which were identified using the automated Thunderstorm Identification, Tracking, Analysis and Nowcasting (TITAN) radar analysis tool (Dixon and Wiener, 1993). Their convective radar echo top height (ETH) statistics showed little evidence for a multimodal distribution as hypothesised by early observations (Johnson et al. 1999) and models (Liu and Moncrieff, 1998). Instead they found a continuous distribution of ETH with the peak of the distribution shifting towards tropical tropopause layer (~15 km) as the distributions are conditioned on higher reflectivity (May and Ballinger, 2007). But they did not provide any information on the variations with respect to underlying surface and local time or the variability with respect to recently identified large-scale atmospheric regimes.

The present paper aims to extend the May and Ballinger (2007) study. The specific objectives of this study are: (1) to assess how the large-scale atmospheric regime affects the distribution of the convective clouds, ETH and associated electrical activity by analysing the diurnal and spatial variability, (2) to examine the variability of convective cell volume, kinematics and cell onset times during the respective large-scale atmospheric regimes and (3) attempt to ascertain the significance of the large-scale regime against other competing factors such as underlying surface and diurnal cycle, in the production of tropical convective clouds. This paper is organised as follows: The datasets, together with the techniques employed to extract convective cloud properties from radar reflectivities are described in section 2. The basic characteristics and spatial variability of convective clouds properties as a function of the large-scale atmospheric regimes is described in Section 3.1, followed by an analysis of the diurnal variability in Section 3.2. Finally, the results are summarized and discussed in Section 4.

2. Datasets and Method

The study makes use of two wet seasons (October 2005 – April 2006 and October 2006 – April 2007) of data from the Darwin C-band polarimetric research radar (CPOL: Keenan et al. 1998), the Australian GPATS (http://www.gpats.com.au/) lightning products and radiosoundings at Darwin airport. The sounding data are from the daily 2300 UTC (0830 LT) operational observations. The 2300 UTC data are selected to avoid modification of the environment by strong diurnal convection.

The CPOL radar (Lat.: 12.25°S, Long.: 131.04°E) as shown in fig. 1, collects a three-dimensional volume of data out to a range of 150 km once every 10 min. Each volume consists of a series of 16 conical sweeps at elevations ranging from 0.5° to 42°. The radar transmits alternate linear horizontal and vertical polarization pulses of wavelength 5.3 cm. The main data source used in the present paper is the three-dimensional radar reflectivity after attenuation by rain is corrected for using the method developed by Bringi and Chandrasekar (2001). Other important polarimetric radar retrievals, such as drop size distribution and precipitating water contents are analysed separately in a paper in preparation.

Figure 1 shows the extent of the domain sampled by the CPOL radar. Only data from the highlighted grey region (radar ranges of 20–120 km) are analysed in this paper. This is done to reduce errors due to limited sample size at close ranges caused by the “cone of silence” occurring at elevation angles greater than 42° and at large ranges due to beam spreading. We also found that the mean radar ETH near maximum range of 150 km is ~1 km higher than the mean ETH within 120 km of radar centre. The radar ETH statistics has a small range bias due to the radar scanning geometry; however, this effect is quite small within our radar sampling domain.

Reflectivity data are gridded by constructing a series of the Constant Altitude Plan Position Indicators (CAPPI) at every 0.5 km in height (with a horizontal bin size of 2.5 km x 2.5 km) extending up to 20 km, using the Sorted Position Radar INTerpolation (SPRINT) software. The gridded reflectivity data at a CAPPI level of altitude 2.5 km are processed using the "Steiner" convective / stratiform classification algorithm (Steiner et al. 1995) to determine the occurrence of the convective and stratiform precipitation at individual radar pixels. The Steiner algorithm classifies the gridded reflectivity as convective if the reflectivity value is at least 40-dBZ or greater than a fluctuating threshold depending on the area-averaged background reflectivity (within a radius of 11 km around the grid point). Each convective centre has a radius of influence (ranging from 1 to 5 km) also depending on the surrounding background reflectivity (Steiner et al. 1995).

For each identified convective pixel at 2.5 km CAPPI level, the maximum height of the 5-dBZ echoes is computed to provide an estimate of the "echo top height (ETH)". Specifically, the ETH corresponded to radar echo height whose reflectivity is the closest to 5-dBZ, but with a reflectivity value within the range of 0-dBZ to 10-dBZ, and provided there are continuous (in the vertical) reflectivity fields between the 2.5 km CAPPI level and this ETH. This procedure filtered out any possible effects of detached cloud layers situated above the convective towers. The 5-dBZ radar ETH definition has been previously used by May and Ballinger (2007).

In most cases, the true cloud top height will extend higher than the 5-dBZ ETH; however, using CloudSat data the difference between cloud top heights and radar 0-dBZ or 10-dBZ ETH has been found to often be within 2 km (Casey et al. 2012). Selecting the lowest available reflectivity per convective column might appear to be a better proxy of cloud top height. However, this will introduce artefacts because the radar sensitivity drops with range, leading to fewer signals detected at longer ranges. The radar detection sensitivity is 0-dBZ near its maximum range of 150 km, so the choice of 5-dBZ threshold is sufficiently high to allow for detection of echoes at any radar range considered in this study.

This study also makes use of cell-based analysis, such as cell lifetime, speed, direction of movement and volume. These parameters are derived using the TITAN radar analysis tool (Dixon and Wiener, 1993). TITAN identifies convective cloud volumes based on radar reflectivity and volume thresholds. It then tracks these cloud volumes (hereafter referred as simply as 'cells') in space at discrete times (every 10 min in this case). Here a minimum volume requirement of 30 km^3 and a reflectivity threshold of 35-dBZ are used to identify convective cells (e.g., May and Ballinger, 2007). To reduce noise, filters are applied to the data. We only use information from cells that could be tracked over at least two consecutive radar scans. Thus, the analysed cells had a minimum lifetime of 10 minutes. Moreover, only cells that formed and decayed within the radar sampling domain are used in the analysis. This is achieved by rejecting any track that passed beyond a 140 km radius (the maximum radar coverage radius is 150 km). Similar TITAN cell selection criteria have been used elsewhere (Goudenhooft et al. 2010). Overall, from a total of 50,485 cells that were detected by TITAN during the two seasons, these filters rejected ~56% of the cells, leaving just over 22,000 cells in our analysis. However, if one chooses to restrict the maximum radius to 120 km, as has been done for the Steiner method, 4,500 more TITAN cells are discarded. Importantly, the TITAN analysis tool does not require gridded radar data, so the interpolation of the observed conical scans into CAPPIs is not a concern, which allows for an investigation of up to 140 km range.

A crucial difference between the Steiner and TITAN methods of convective cell identification is that the former is likely to capture small cells such as those in the early growth or decay phase as well as mature cells, whilst TITAN has been designed to find mostly mature, intense cells. This is because the Steiner method does not have a minimum volume or lifetime requirement and permits lower reflectivities in the analysis (Steiner et al. 1995).

Finally, the electrical properties of the convective clouds are estimated using GPATS lightning data. Similar to other lightning detection networks, the GPATS network uses GPS-synchronised time stamps of the observed lightning sferics signals from each station and locates the strokes using the time of arrival method. To study the response of lightning associated with convective clouds, a lightning stroke was only used for the subsequent analysis provided there was at least one convective pixel occurring within a radius 10-km in distance and 10-min in time of this lightning stroke. These criteria rejected ~6 % of strokes, from a total of 153,125 strokes detected within the radar domain over the two seasons.

In the subsequent analysis, the lightning occurrences are expressed in units of flashes per minute per pixel/cell. Several thousands of convective pixels had no lightning stroke associated with them and these '0' flash rates are retained during the calculation.

3. Results

3.1 Basic convective clouds characteristics during the different large-scale atmospheric regimes

a) Mean regime characteristics

This section provides an account of the average cloud characteristics and associated electrical properties (Table 1), together with horizontal wind vectors, vertical shear of horizontal winds (hereafter, vertical wind shear) and vertical profile of humidity profiles (Fig. 2) for the five large-scale atmospheric regimes identified by Pope et al. (2009a). The long-term thermodynamic profiles and the large-scale environment are described in Pope et al. (2009a). Note that their details, but not their broad-scale characteristics, will differ somewhat from our results due to interannual variability. The vertical wind shear profile complement results from Pope et al. (2009a), as wind shear has long been known to have an impact on convective organization, strength and propagation properties (e.g. Rotunno et al. 1988).

Table 1 shows the 95% confidence interval range of the number of Steiner identified convective pixels and TITAN cells, together with the lightning flash rate per pixel/cell as a function of the large-scale atmospheric regime. As TITAN keeps track of cell splits and mergers during successive radar volume scans, cell identification can be complex. Here, all cells that had the same 'complex track identification number' are treated as one cell. The complex track number remains the same even if the cell splits or merges during its lifetime. For study period, 78% of the detected TITAN tracks have a simple structure free of any splitting or merging events. The remaining 22 % of cells have a complex structure, with a majority of them undergoing cell mergers. Merged cells are typically taller and larger than simple cells (Westcott, 1994). The Steiner method treats each individual radar pixel independently.

Note that the 95% confidence interval of the convective occurrence frequency for the respective regimes does not overlap when using the Steiner method (Table 1). This is an initial indication that significantly different convective occurrence patterns do occur during the five large-scale regimes. Differences in convective cloud properties such as cell volume, propagation speed and lifetime are significant when one compares the results of the Deep Westerly (DW) regime (corresponds to the active monsoon period) against that of the other regimes.

The Dry Easterly (DE) regime may be viewed as the trade wind regime. It mainly occurs in October and November (Table 1). The winds are southeasterly in this regime at low altitudes (Fig. 2a), reversing to westerly at ~8 km and back to easterly above 16 km height. The upper level (> 15 km) easterly winds occur persistently in all regimes and are due to the presence of an upper-level jet. The DE regime has cells which typically lasted longer than other regimes. This could be due to the strongest low-level (0 – 3km) and mid-level vertical wind shear (Fig. 2b). Robe and Emanuel (2001) and several earlier studies indeed suggested that strong shear in the lower levels produced more organised and longer lived convection. Both the Steiner and TITAN methods show that this regime has the lowest rate of convective activity however; the lightning flash rate per convective pixel or cell is the highest. Low convective cloud activity is consistent with lowest relative humidity (Fig. 2c), which is due to a dry continental air mass being advected over Darwin (Pope et al. 2009a). The existence of higher lightning flash rates during pre-monsoon (and monsoon break) conditions, than during the active monsoon period, has been previously documented over Darwin using lightning data from a separate lightning network (Höller et al. 2009; Labrador et al. 2009). Overall, the DE regime occurs ~11 % of the time in our two-season sample and contains only very few detectable radar convective pixels (on average 312 pixels per day). We, therefore, choose not to show any further results from this regime from hereon.

The Easterly (E) regime is typically seen as the transition between the trade wind regime and monsoon onset. It occurs mainly in the early and late part of the wet season. For the study period, this regime is the least frequent and accounts for only 7 % of our total sample. The E regime has a higher average number of both convective pixels and cells than the DE regime, but still smaller compared to the other regimes. The large-scale synoptic environment advects an airmass from the Coral Sea over Darwin (Pope et al. 2009a), which creates a moister environment than that of the DE regime (Fig. 2c). The horizontal wind vectors and vertical shear wind profile are similar to the DE regime except in the mid-troposphere (8–15 km) where they are much weaker in the E regime (Fig. 2a and 2b). The lightning flash rate per pixel is moderately high in this regime and is consistent with pre-monsoonal lightning features (Höller et al. 2009; Labrador et al. 2009).

The Deep Westerly (DW) regime is associated with typical monsoon conditions, and its occurrence peaks between January and March (Table 1). It accounts for 18 % of the total sample. The large-scale synoptic environment indicates the presence of northwesterly winds at low levels (Fig. 2a) transporting an airmass of equatorial origin into the region (Pope et al. 2009a). They also found that this regime produced the highest amount of rainfall consistent with the highest relative humidity of all regimes (Fig. 2c). Both the Steiner and TITAN methods reveal that the DW regime generates the highest convective area and cell counts per day, respectively. However, the mean volume of the convective cells in the DW regime is relatively small, ~68 km^3, compared to the other regimes with a mean cell volume of close to ~100 km^3. This may be partly because ~90% of cells in this regime have simple track structure, whereas the other two convective activity regimes (SW and ME, described below) have only 67–70 % cells as simple. Also, the low and mid-level vertical wind shear is weakest in this regime, so the convection is predicted to be relatively short-lived (e.g. Table 1) and less organised (e.g. Rotunno et al. 1988; Robe and Emanuel, 2001). Consistent with previous studies, the DW regime is found to have the least amount of lightning discharges (Höller et al. 2009; Labrador et al. 2009).

The Shallow Westerly (SW) regime has previously been found to occur when the active monsoon region moves to the east of Darwin (Pope et al. 2009a). They found this regime to be associated with the largest mean CAPE (Convective Available Potential Energy) values of about 1100 J kg^{-1} and potentially stronger updrafts. The SW regime occurs 16 % of the sample time. Table 1 shows that the SW regime has the second highest convective area per day and similar number of convective cells as the moist easterly regime (ME, described next). The SW regime is found to have the highest percentage of cells undergoing merger. Also, the electrical activity is consistently higher than in the other two frequently occurring regimes (DW and ME) regardless of the data processing procedure. The wind vectors in the SW regime change fairly rapidly in the first 2 km, veering from westerly near the surface to southerly at ~ 2km (Fig. 2a). Between 2 – 8 km, the winds in the SW regime continued to be southerly and then strongly easterly above 15 km height. The rapid changes in the near-surface winds caused the low-level shear in the SW regime to be approximately 7 times more than in the DW regime (Fig. 2b). The relative humidity level is slightly less than that observed during the DW regime (Fig. 2c).

The Moist Easterly (ME) regime can be viewed as the typical break monsoon period. This regime is the most frequent, occurring 48 % of the sample time, and could be interpreted as the “default” state of the Darwin wet season. The convective area and cells numbers are similar to the SW regime but electrical activity seems to be slightly lower. The large-scale synoptic environment indicates the presence of easterly wind anomalies transporting an airmass of equatorial origin, together with large region of convergence over Darwin (Pope et al. 2009a). The sounding data (Fig. 2a) highlight the presence of easterly winds extending throughout the troposphere with lowest wind magnitude near ground level and at ~10 km. The low and mid-level vertical wind shear is moderately high in this regime, and therefore favours more organised convection compared to the DW regime.

b) Convective 5-dBZ echo top heights and associated lightning

This section shows the overall variation of the 5-dBZ ETH extracted using Steiner convective pixels and associated lightning as a function of large-scale atmospheric regime. The diurnal features of these two cloud properties are in section 3.2b. Figure 3a shows the probability distribution function (PDFs) for ETH using 1-km bins in height for the four regimes with sufficient samples (E, DW, SW and ME). The shaded grey region in this figure and all subsequent figures is the average distribution obtained using data from all days, regardless of regime classification. Figure 3b shows the vertical profile of the lightning flash rate per pixel.

The ETH distribution for all convective pixels (grey shaded region) shows a broad peak between 8 and 14 km (Fig. 3a). Each large-scale atmospheric regime shows a single peak occurrence in the ETH. There is no clear evidence of a multimodal distribution of convective ETH as reported by previous studies (e.g. Liu and Moncrieff, 1998; Johnson et al. 1999) even though a significant amount of cumulus congestus cloud is present in our analysis. Our analysis is unable to reproduce the trimodal distribution of Johnson et al. (1999) because: 1) each individual convective cloud could have several ETH which will smear out the less dominant peak occurring near the tropopause layer (~15 km). Our main goal here is to study the convective fractions, so ETH data are considered more suitable than cloud top height (CTH); and 2) the shallow cumulus clouds with peak heights within 1–2 km are usually missed because they are typically non-precipitating and so cannot be captured with our C-band radar due to minimum detectable signal and sampling issues. However, there seems to be some evidence of a multimodal peak in convective ETH when it is presented as a function of diurnal cycle (see Fig. 11).

Figure 3a shows that the E regime (black) has the peak occurrence at the lowest height of all regimes (~8 km), followed by the DW regime (~11 km). The deepest convective clouds form in the SW regime with a peak occurrence at ~14 km and could be associated with stronger updrafts (e.g. Pope et al. 2009a). The mean distribution (grey shaded region) and the ME regime are mostly similar, since the ME regime is by far the most frequent (see Table 1). The TITAN method also produces the same dependence of ETH on large-scale regime except that the occurrence peak height is higher by 1 – 2 km (not shown).

The lightning occurrence profiles (Fig. 3b) show that the lightning rates increase strongly with convective ETH, with all but the DW regime showing the most lightning for the deepest clouds. The convective clouds in the E regime produce about 2 – 3 times more lightning than other regimes for all ETH up to a height of ~15 km. Notably, the SW regime has a secondary peak in lightning production rate associated with ETH around 10 km (Fig. 3b). In general, lightning is believed to be triggered when there is interaction between upward flux of supercooled liquid water and downward flux of graupel in the mixed phase (−10°C and −40°C) of thunderstorms

(Deierling et al. 2008). To maintain this process, sufficient CAPE to support vertical motions in excess of 6–7 m s^{-1} is required to supply supercooled liquid water in mixed phase (van den Broeke et al. 2005). Large CAPE values potentially lead to stronger updrafts and higher ETH, so it is logical to expect the lightning flash rates to increase with ETH.

Figure 4 provides the spatial distribution of the average ETH, convective cloud occurrence frequency and associated lightning flash rates. All data in this figure are interpolated to a 5 km x 5 km grid. We notice that the average ETH (top panels) is slightly higher beyond the ranges of 120 km (not shown) due to the beam spreading effect. Small size convective cells (which are typically shallow in height) with narrow horizontal cross-sectional area become less frequent as the horizontal distance between adjacent beams widen at further ranges because they are likely to be missed during the SPRINT interpolation. As a result mostly wider, taller cells contribute to the mean ETH near the maximum sampling range.

During the E regime (left column) a maximum in convective clouds is found over the ocean. The oceanic clouds in this regime generally have a higher mean ETH of ~10.5 km, compared to those occurring over land, whose average height is ~8 km. The lightning occurrence peaks tend to be collocated with regions of higher average ETH, with a significant proportion occurring along the coastline. Data from lightning networks have also shown significant lightning along the Top End coastline of Darwin (e.g. Labrador et al. 2009).

During the DW regime the convective cloud occurrences are found to be larger over the western half of the domain, with the majority of them occurring in the Beagle Gulf (see Fig. 1 for location) and its coastal boundary regions. This region has been shown to have maximum precipitation during Darwin monsoon periods (May et al. 2012). The mean ETH is ~10 km, which is low compared to the other convectively active regimes (SW and ME), but convective cloud occurrence rate, especially over the ocean, is highest in this regime. This may be because during the DW regime, convection is embedded in a large-scale ascending region associated with the monsoon trough (May et al. 2012). The lightning locations are generally widespread and low in occurrence, with a maximum lightning occurrence being collocated with the maximum occurrence of convective cells.

A comparison of the spatial maps of the SW regime against the DW regime suggests that the peak convective occurrence locations show some tendency to shift eastward, from the western half in the DW regime to the region within 50 km surrounding the radar centre. This is consistent with the conjecture that during the SW regime, the active monsoon region has moved to the east of Darwin (Pope et al. 2009a). The mean ETH is clearly the highest of all the regimes. The lightning occurrence rate is also the higher in this regime compared to the DW regime, with the maximum lightning occurrence located mainly over the ocean. Possible reasons for the higher lightning occurrence over the ocean than the land are discussed in section 3.2. A closer examination of radar reflectivity loops and lightning occurrence reveals that the observed lightning occurrence peak is due to a significant number of events, not just a few extreme events.

During the most common regime (ME), maximum convective cloud occurrences are on the western part of the Tiwi islands, consistent with the frequent occurrence of Hector storms (e.g., Carbone et al. 2000). Early storms typically occur over the eastern part of the Tiwi islands and propagate westward during the break monsoon conditions. Carbone et al. (2000) explains that these storms intensify as they approach the west coast due to cell merger, and so more convective pixels are detected by the radar on the western part of Tiwi islands. However, these Hector storms do not seem to be as electrically active as storms forming along the Top End coastline. Focusing only over the Tiwi islands, the lightning flash rate per convective pixel seems to the highest along the west coast region where cell merger is most likely to occur. This is consistent with the electrical activity associated with typical Hector storms (Carey and Rutledge, 2000). They found no significant lightning during developing stage of Hector storms and maximum flash intensity associated with cell merger during the mature phase. The mean ETH shows moderate dependence on the underlying surface, with ETH slightly higher over the mainland than over ocean and Tiwi islands. The convective activity is minimum in northeast of Darwin in this ME regime.

Overall, the results shown in Fig. 3 and Fig. 4 indicate that convective cloud occurrence, ETH and associated lightning depend both on the large-scale atmospheric conditions (as exemplified by the Pope et al. (2009a) regimes) and the underlying surface. In the next sections, we investigate the effects of these two factors on other properties of convective cells such as cell lifetime, propagation parameters, volume and cell genesis time. These cell properties are derived using the TITAN analysis tool.

c) Convective cell kinematics

The aim of this section is to examine the variation of convective cell kinematics (i.e., cell lifetime, speed, direction, displacement) obtained using the TITAN tool and their spatial distribution in the four large-scale atmospheric regimes. Results for the DE regime are again not presented because on average this regime had 2 TITAN cell tracks per day. In all four regimes, the cells are mostly short-lived with a mode occurrence lifetime of 20 mins and a strongly positively skewed duration frequency (Fig. 5a). Longer lived cells, such as those with lifetime exceeding 100 mins (~5 % of all TITAN cells), are found to be least frequent in the DW regime.

In contrast, the cell speed varied significantly during the respective regimes (Fig. 5b). The easterly regimes (E and ME) exhibit a much narrower distribution of cell speed with a peak occurrence near 3 m s^{-1}. However, the westerly regimes (SW and DW) are characterized by a broader distribution, with 30 % (15 %) of the cells in the DW (SW) regime having cell speeds exceeding 10 m s^{-1}. This greater cell speed in the westerly regime, particularly the DW regime, is because the steering flow speeds (wind speed at 700 hPa or ~3 km, see Fig. 2a) are larger in those regimes.

Figure 6 shows spatial maps of the cell track distribution and their average displacement, lifetime and speed, as a function of regime. The cell displacement is calculated as follows. First, the coordinates of the cell centre at first detection (t = 0 hrs) are grouped into 20 km x 20 km bins with respect to radar centre. A 20 km x 20 km bin size is chosen to give at least 5 TITAN tracks per bin. Then for all cells in a bin the average location of the cell centre at decay (t = termination of cell) is calculated. The average displacement vector is then defined as the position of cell decay relative to its onset and is shown as an arrow for each bin in the third panels of Fig. 6.

The spatial distribution of the TITAN tracks (top panels in Fig. 6) is similar to the distribution of convective pixels (second panels in Fig. 4). The most noticeable difference occurs in the ME regime, with the western part of Tiwi islands showing comparatively less TITAN tracks than convective pixels. This can be explained since the TITAN occurrence maps show a given track only once at cell onset. As indicated above, the western island maximum found by the Steiner method represents Hector storms, which are usually born on the eastern part of the Tiwi islands and then they propagate westward where the sea breeze interaction makes them more intense (Carbone et al. 2000).

According to the bottom three panels in Fig. 6, cells tend to propagate for larger distances in regions located on the windward side of the incoming large-scale atmospheric circulation. For example, cells located in the northwest half of the domain in the DW regime and those in the southeast half in ME regime propagated for longer distances since they last longer and/or propagate faster. The steering flow mainly controls the direction of propagation of the TITAN cell but it cannot explain the gradual drop in the cell propagation distance as they move from the windward side to the leeward side. The hypothesis that this gradual drop in cell propagation is an artefact because fast moving and long-lived cells are more likely to be filtered out from the leeward side by our cell selection criteria (since they are more likely to propagate beyond 140 km from the radar centre) was investigated and rejected. A similar result is obtained when we used all cells, even those that extended beyond 140 km from the radar centre.

To further investigate this, we calculated spatial variation of the percentage of cells rejected compared to all cells when using a 140 km maximum radius requirement (provided the cell lifetime was at least 10 min). The results of this analysis are shown in the second panels of Fig. 6. It shows that our filters rejected less than 2 % of cells in the circular region of radius 100 km bounded by the second concentric ring. Importantly this region does not show any spatial gradient in the cell rejection frequency, but we still observed longer propagating cells on the windward side compared to the leeward side in this inner region. Analysis of the spatial variation of the ratio of merged cells to all cells (results not shown) indicated that cell mergers on the windward side tend to be higher than on the leeward side. This result supports the observations of longer lived cells (e.g. Westcott, 1994). High resolution 3-D winds and gridded thermodynamic profiles for the region around Darwin would be needed to further understand the salient cloud physics causing this effect, which will be the subject of further investigations.

d) Convective cell volume

The aim of this section is to examine the variation of convective cell volume and its spatial distribution with large-scale atmospheric regime.

The SW and ME regime show a similar distribution of TITAN cell volumes (Fig. 7), with both the DW and E regimes deviating from the mean distribution more significantly. The proportion of cells with a small volume of 30 km^3 is ~15 % for the SW and ME regimes, while it is much larger (~ 22%) for the DW regime and smaller (~ 11 %) for the E regime. Bigger volume cells are most frequent in the E regime, though results are drawn from a smaller number of events. Within the convectively active regimes (DW, SW, and ME), cells with a large volume are more frequent in the SW regime (55 % of the cells had volume > 60 km^3) and ME (51 %) regimes compared to the DW regime (37 %). An interesting feature of the SW and ME regimes is that the cells over land have a larger volume compared to those occurring over ocean (Fig. 8). In contrast, in the DW regime the cell volume shows little dependency on the underlying surface. The drop in cell volume at the far southeast of Darwin could be an artefact associated with increase in the rejection of TITAN cells by our filters (second panels Fig. 6). Overall, this points out that the convective clouds in the DW regime are embedded within the large-scale monsoon trough.

Overall, the variability in cell volume is linked to both the large-scale atmospheric circulations and the nature of the underlying surface. For example, cell volume is largest in the E regime, smallest in the DW regime and intermediate in the SW and ME regimes. Comparing the three most frequent regimes, they all, except for the DW regime, have larger cells over the continent than over the ocean. Since cell volume (Fig. 8) reveals a similar response as the cell area (results not shown here) and to some extend as the ETH (Top panels Fig. 4), it is fair to assume that cells with larger volume will have a greater mean ETH and a wider horizontal extent.

3.2 Effects of the large-scale regime on the diurnal cycle of convection

Having identified significant differences in basic cloud cell characteristics for the four large-scale regimes used in this study, this section focuses on the diurnal cycle of cell characteristics, in particular convective ETH occurrence and associated lightning, as they are indicative of the intensity and microphysical characteristics of the convective systems.

a) Convective cell onset time

In this section we examine variation in cell onset time by binning the onset times with respect to the Darwin local time (LT = UT + 09:30). The distribution of cell onset times (Fig. 9) shows that most of the cells are triggered during the day with a secondary peak occurring in the early morning period. For the DW regime, the daytime peak of the cell onset occur the earliest, around midday, followed by the SW regime at 14:00 LT and around 15:00 LT for the easterly regimes.

The spatial maps of the cell onset times (Fig. 10) show well-defined differences in the dominant local time of the onset of convective cells with respect to the underlying surface. Some caution must be exercised when interpreting the results shown in Fig. 10, as the colours only represent the modal local time of the onset of convective cell development. Obviously some cells will be born outside the modal local time period for a given underlying surface. Over the ocean, the cells are triggered mainly in the early morning and in some cases around midnight, regardless of the regime type. Over land, the cells are predominantly triggered in the afternoon except for the DW regime. In the DW regime, the triggering of the cells within ~60 km from the coast line happens around midday, while for the remaining land region it still occurs in the afternoon. These features in the diurnal cycle of cell onset time with respect to different underlying surface type are consistent with earlier research (Liu and Zipser, 2008 and references therein).

In all regimes except the DW regime, convective cells over land are likely initiated by sea breezes whereas ocean cells are predominantly triggered by the land breeze. Thus, the cell onset times are strongly dependent on diurnal cycle and on the underlying surface, in at least three out of four regimes. In contrast, in the DW regime (or monsoon period) with extensive cloud cover, radiative heating of the land is less effective resulting in changes to the mechanisms that trigger convection (May et al. 2012).

b) The diurnal cycle of convective ETH

Figure 11 shows the evolution of ETH occurrence frequency as a function of time of day and height for each of the large-scale regimes. The ETH occurrences are calculated separately for each bin of 1-hr in local time and 1-km in height, and then normalised by the number of days in each regime. For clarity, the counts are then further divided by the peak occurrence value in each panel (peak values given on the bottom right hand corner). The density of points as a percentage of the maximum occurrence is presented using a colour scale with white indicating that no data is recorded in this bin.

In the E regime convective echo occurrence is highest in the afternoon and in the early morning period (Fig. 11). It appears that, especially in the afternoon period, the clouds are generally shallow during the early growth phase and progressively develop into deeper clouds in the mature stage. This diurnal cycle is consistent with that of the non-precipitating ice clouds over Darwin during that same regime, as characterized in Protat et al. (2011). This consistency suggests that in the E regime, non-precipitating ice clouds are predominantly convectively generated. At all times, except for the afternoon period, mean ETH (black curve) during the E regime is lower than the mean values for all regimes (black-white dashed curve). The electrical activity in the E regime is semi-diurnal and follows the convective echo occurrence frequency, with the lightning flash rate peaks occurring fewer hours prior to peaks in convective ETH occurrence (white curve).

The DW regime shows a prolonged period of occurrence of convective clouds from midnight through the morning with a peak around midday, and a clear occurrence minimum in the evening (Fig. 11). Typically during monsoon conditions, which the DW regime represents, there is a large proportion of stratiform clouds (May and Ballinger, 2007). Hence the convective ETH diurnal cycle is expected to deviate from that of rainfall, which often shows a maximum in the afternoon and evening. Overall, the average ETH of ~10 km is generally lower than in the all regime average. The DW regime is the least active in terms of lightning and this could be due to insufficient updraft speeds within the convective core to produce lightning (e.g. van den Broeke et al. 2005). Unlike the E regime, the frequency of occurrence of non-precipitating ice clouds in the DW regime in Protat et al. (2011) is very different from the convective ETH statistics obtained here. The maximum in non-precipitating ice cloud occurrence occurs later than the convective ETH occurrence maximum, between 15:00-20:00 LT (Fig. 2d in Protat et al. 2011). This comparison suggests that during the DW regime, thick non-precipitating anvils and cirrus decks produced by deep convection are much longer-lived than during other regimes. During the DW regime, the diurnal variation in atmospheric temperature is weak due to widespread cloud cover reducing the daytime heating of the land (May et al. 2012). This largely explains the lack of a strong evening peak in the occurrence of convection during this regime.

During the SW regime the average ETH is higher than the mean values for all regimes at all times of the diurnal cycle, with two peaks, one in the morning and one in the afternoon. We previously have shown that the SW regime also contains the tallest convective ETH (Fig. 3a) and with moderate cell volume (Fig. 7) possibly due to stronger updrafts and increased occurrence of cell merging. The peak in non-precipitating ice cloud occurrence (Protat et al. 2011) is shifted to a later time (20:00-24:00 LT), suggesting again the production of extended anvils by deep convection associated with the SW regime, as is the case for the DW regime as well. The SW regime is found to have the second highest lightning activity, with the majority of lightning strokes generated by the early morning storms. Again the peak in lightning flash rates tends to occur few hours ahead of the peak in convective ETH occurrence.

During the most frequent ME regime, the results reveal that the early phase of storm development occurs at ~15:00 LT with a peak height of 9 km (Fig. 11). These cells mature within a few hours, becoming towering cumulonimbus clouds with a peak occurrence height of 14 km. This diurnal cycle is consistent with that of the non-precipitating ice clouds (Protat et al. 2011) in this regime. This suggests that thick anvils and cirrus decks produced by deep convection are shorter-lived than during the DW and SW regimes. From the evening through the night the convective systems gradually decay causing a gradual drop in ETH. This drop is also found in the non-precipitating ice cloud statistics (Protat et al. 2011). The infrared satellite observations analysed by Pope et al. (2009b) confirm a mesoscale convective system genesis time near 15:00 LT during monsoon break periods, and these usually decay within approximately 3 hrs. The lightning flash rates are highest when the ETH reached the peak heights in the evening period.

A shortfall in Fig. 11 is that the responses in ETH may be affected by the complex topographic environment around Darwin. We attempt to rectify this by further splitting the time-height pdfs of ETH into three groups of different underlying surface types, namely oceanic, coastal and continental. The results are shown in Fig. 12 and the area covered by the three surface types is shown in Fig.1. In the DW regime (Fig. 12a), the peak occurrence in convective clouds occurs earliest over the oceanic surface in the early morning period and progressively shifts inland, peaking over the continental surface near midday. This progression of convective cloud activity from the oceanic region through coastal and then over land is consistent with the picture that convection in the DW regime is embedded in the large-scale forcing by the monsoon trough. In contrast, convection in the ME regimes seems to be primarily dependent on conditioning of the atmosphere by land and sea breeze processes. For example, the majority of convective cloud activity occurs above the oceanic region in the early morning period, with peak heights at 14 km. In contrast, during the afternoon and evening periods, the convective cloud occurrence is highest above the coastal (bimodal peak height of 9 and 14 km) and continent (peak height of 14 km) regions, respectively. There is little evidence to suggest that the early born coastal convection is progressing over the continent since storms in the ME regime mainly propagate towards the ocean (see Fig. 6). Results for the E and SW regimes are not shown because they exhibited less noticeable differences in the convective cloud occurrence over the three underlying surfaces.

Overall, the results shown in Fig. 11 and Fig. 12 indicate that the diurnal cycle of convective cloud occurrence and their top heights, and spatial location of the convective clouds, contrast considerably amongst the four large-scale atmospheric regimes. Firstly, all the regimes, except the DW regime, show intense convective activity in the late afternoon, presumably initiated by the sea breeze circulation that forms on the Top End coastline. The results also indicate that sea breeze effects are less important during the DW regime. Secondly, the DW regime clearly shows oceanic characteristics, while the ME regime demonstrates much more continental characteristics. Thirdly, the SW regime (and the E regime, though results are drawn from a smaller number of events) show high convective activity after midnight and in the early morning, thus showing that convection in this regime exhibits somewhat oceanic characteristics. Finally, the comparison of the diurnal cycle non-precipitating ice clouds and convective cloud towers indicate that the thick anvils and cirrus decks produced by deep convection are shorter-lived during easterly regimes (E, ME) and longer lived during the westerly regimes (DW, SW).

Higher lightning flash rates after midnight (vs. afternoon or evening), particularly in the E and SW regime, and over the coastal boundary region (vs. continent) do not seem to be consistent with the traditional picture of having more lightning over land and in afternoon period. The complex topography of coastlines, islands and oceanic areas within our sample area combined with the distinct wet regimes may be contributing towards this discrepancy. On the other hand, since the Darwin site with its Doppler radar pair can provide higher resolution 3-D wind data, it will offer an opportunity in the future to derive upward mass fluxes and to check consistency with lightning activity (e.g., Deierling et al. 2008). The question is: for a given mass flux rate, do convective cells produce more lightning when located over land (vs. sea) or in afternoon period (vs. early morning period)? This is the subject of ongoing investigations.

4. Conclusion and Summary

Polarimetric weather radar data collected over two wet seasons (October 2005 – April 2006; October 2006 – April 2007) at the tropical low-latitude station of Darwin, Northern Australia, are used to study the variability of convective cloud properties with both the large-scale state of the atmosphere, the diurnal cycle, and the underlying surface type. The properties of convection studied here include the frequency of convective cloud occurrence, 5-dBZ echo top heights (ETH), kinematics (lifetime, speed and direction of propagation), cell structures and volumes. Both the spatial and diurnal variability of these tropical convective cloud properties are studied as a function of the identified main large-scale atmospheric states in this area.

A summary of the key findings is as follows:

1. The most frequent ME (break) regime shows highest convective activity from afternoon to midnight and a secondary occurrence peak in early morning. These convective clouds occur most frequently on the western part of Tiwi islands, which is consistent with the signature of the well-known Hector storms. In the afternoon the convective clouds are initially shallow with a modal height of ~9 km, and within a few hours grow into deeper convective towers with a modal height of ~14 km. The ETHs are higher and the cloud cell volumes are larger over land than sea. It is also very clear from the results that the land cells in this regime are predominantly initiated in the afternoon by sea breeze processes whereas ocean cells pop up in the early morning due to land breeze effects. Overall, the convection in the ME regimes seems to be well organised and shows characteristics similar to continental convection. Since this regime occurred for nearly 48% of the wet season, its convection patterns could be a fair representation of the default climatology of Darwin.

2. In contrast, the DW regime, which corresponds to the active monsoon period, exhibits the highest overall probability of generating convective cells. It has a peak convective cloud occurrence over the coastal boundary region from midnight to early afternoon. The evening convective activity is least frequent in this regime and is thought to be due to the presence of continuous cloud cover reducing daytime heating that prevents the establishment of sea breeze convergence. The vertical wind shear in the low-levels, convective ETH, cloud cell volumes and lightning activity are all smaller in this regime compared to the other convectively activity regimes (SW and ME regimes). Also, the effect

of the underlying surface types on most convective cloud properties is the weakest in the DW regime. Overall, clouds in this regime exhibit oceanic characteristics, with convection being embedded in the large-scale forcing of the monsoon trough.

3. In the SW regime, the peak convective occurrence location shifts eastward compared to the DW regime. This observation supports the hypothesis that these two regimes are connected to the eastward propagation of the monsoon trough. Another feature in the SW regime that matches with the DW regime is the increase in occurrence of convective clouds in the early morning period. However, unlike the DW regime, the effect of the underlying surface on the convective cloud properties is somewhat strong in the SW regime. For example, the land cells predominantly initiate in the afternoon and have a larger volume compared to those that form in the early morning over the ocean. Another contrasting feature is the convective cloud activity in the SW regime is moderately high in the afternoon. Overall, this indicates that the SW regime are regulated by a mixture of large-scale forcing that are important for the DW regime and the sea-breeze effects that dominate the ME regime.

4. The E regime behaves in a similar manner as the SW regime. Like to the DW regime, the E regime has the highest convective cloud activity in the early morning period. While the observed secondary peak in convective cloud activity in the evening period can be attributed to the sea breeze effects. The effect of the underlying surface on the convective cloud properties is moderate. Contrary to the SW and ME regimes, the E regime has somewhat higher ETHs and larger cloud volumes over ocean than land. The convective

clouds in this regime have one of the highest tendencies of producing lightning flashes, and most of these electrically active clouds are located at the Top End of the Darwin coastline.

The main purpose of the study was to use the complex meteorological and topographic environment around Darwin to study the relative influence of the large-scale atmospheric conditions, as represented by a set of synoptic regimes, and the underlying surface types on the basic characteristics of convective systems and their diurnal evolution. The picture emerging from this study shows an intricate interplay between large-scale regime and surface type influences on the properties of convection. To first order, the large-scale regime determines much of the convective evolution, as exemplified by the rare occurrence of convection in the E and DE regimes, and the widespread occurrence of relatively weak convection in the DW regime. However complex topography, such as the presence of coastlines, is a major secondary factor in determining the structural characteristics of convection. For example, during the ME regime, much of the convection triggers along sea-breeze fronts either over the Tiwi islands or the mainland. This indicates that the large-scale state does not allow convection to occur spontaneously over the ocean, but does allow for more organized forms of convection. This picture is likely typical not only for the North of Australia, but the entire Maritime Continent, where the existence of numerous islands of varying size can trigger sea-breeze convection even in large-scale conditions unfavourable for widespread convection over oceanic areas. In contrast, during the DW regime, the surface influence becomes negligible, as the large-scale upward motion associated with the monsoon trough provides sufficient forcing to allow widespread convection with large areas of long-lived stratiform cloud, which in turn suppresses the daytime heating of the land.

Acknowledgements

This work has been supported by the US Department of Energy ARM. We would like to acknowledge the contributions of Brad Atkinson and Michael Whimpey in supporting the Darwin observatory and data management. Rodney Potts and Kevin Cheong are thanked for providing the TITAN data and discussion on it. James Sofra for GPATs lightning data. Special thanks to Susan Rennie and Surendra Rauniyar for their discussion and comments.

References

Bringi, V. N., and V. Chandrasekar, 2001: Polarimetric Doppler weather radar: Principles and Applications. Cambridge University Press, 636 pp.

Carbone, R. E., J. W. Wilson, T. D. Keenan, and J. M. Hacker, 2000: Tropical island convection in the absence of significant topography. Part 1: Life cycle of diurnally forced convection. Mon. Weather Rev., **128,** 3459–3480.

Carey, L. D., and S. A. Rutledge, 2000: The relationship between precipitation and lightning in tropical island convection: A C-band polarimetric radar study. Mon. Weather Rev., **128,** 2687–2710.

Casey, S. P. F., E. J. Fetzer, and B. H. Kahn, 2012: Revised identification of tropical oceanic cumulus congestus as viewed by CloudSat. Atmos. Chem. Phys., **12,** 1587-1595.

Deierling, W., W. A. Petersen, J. Latham, S. Ellis, and H. J. Christian, 2008: The relationship between lightning activity and ice fluxes in thunderstorms. J. Geophys. Res., **113**, D15210, doi:10.1029/2007JD009700.

Dixon, M., and G. Wiener, 1993: TITAN: Thunderstorm identification, tracking, analysis, and nowcasting - a radar-based methodology. J. Atmos. Oceanic Technol., **10,** 785–797.

Goudenhoofdt, E., M. Reyniers, and L. Delobbe, 2010: Long term analysis of convective storm tracks based on C-band radar reflectivity measurements. 6th European Conference on Radar in Meteorology and Hydrology, Romania, 1-7.

Höller, H., H.-D. Betz, K. Schmidt, R. V. Calheiros, P.T. May, E. Houngninou, and G. Scialom, 2009: Lightning characteristics observed by a VLF/LF lightning detection network (LINET) in Brazil, Australia, Africa and Germany. Atmos. Chem. Phys., **9**, 7795-7824, doi:10.5194/acp-9-7795-2009.

Jakob, C., 2003: An Improved strategy for the evaluation of cloud parameterizations in GCMs. Bull. Amer. Meteorol. Soc., **84**, 1387-1401.

Jakob, C., 2010: Accelerating progress in global atmospheric model development through improved parameterizations - Challenges, opportunities and strategies. Bull. Amer. Meteorol. Soc., **91**, 869-875.

Johnson, R. H., T. M. Rickenbach, S. A. Rutledge, P. E. Ciesielski, and W. H. Schubert, 1999: Trimodal characteristics of tropical convection. J. Climate, **12,** 2397–2418.

Labrador, L., G. Vaughan, W. Heyes, D. Waddicor, A. Volz-Thomas, H.–W. Pätz, and H. Höller, 2009: Lightning-produced NO_x during the Northern Australian monsoon; results from the ACTIVE campaign. Atmos. Chem. Phys., **9**, 7419-7429, doi:10.5194/acp-9-7419-2009.

Liu, C., and E. J. Zipser, 2008: Diurnal cycles of precipitation, clouds, and lightning in the tropics from 9 years of TRMM observations. Geophys. Res. Letters, **35**, L04819, doi:10.1029/2007GL032437.

Liu, C. and M. W. Moncrieff, 1998: A Numerical study of diurnal cycle of tropical oceanic convection. J. Atmos. Sci., **55**, 2339 – 2344.

Keenan, T. D., K. Glasson, F. Cummings, T. S. Bird, J. Keeler, and J. Lutz, 1998: The BMRC/NCAR C-band polarimetric (CPOL) radar system. J. Atmos. Oceanic Technol., **15,** 871–886.

Keenan, T. D., and R. E. Carbone, 1992: A preliminary morphology of precipitation systems in tropical northern Australia. Quart. J. Roy. Meteor. Soc., **118,** 283–326.

May, P. T., and A. Ballinger, 2007: The statistical characteristics of convective cells in a monsoon regime (Darwin, Northern Australia). Mon. Wea. Rev., **138**, 55-73.

May, P. T., C. Long, and A. Protat, 2012: The diurnal cycle of the boundary layer, convection, clouds, and surface radiation in a coastal monsoon environment (Darwin Australia). J. Climate. doi:10.1175/JCLI-D-11-00538.1, in press.

May, P. T., J. H. Mather, G. Vaughan, C. Jakob, G. M. McFarquhar, K. N. Bower, and G. G. Mace, 2008: The Tropical Warm Pool International Cloud Experiment. Bull. Amer. Meteor. Soc., **89**, 629-645.

Pope, M., C. Jakob, and M. Reeder, 2009a: Regimes of the north Australian wet season. J. Climate, **22**, 6699-6715.

Pope, M., C. Jakob, and M. Reeder, 2009b: Objective classification of tropical mesoscale convective systems. J. Climate, **22**, 5797-5808.

Protat, A., J. Delanoë, P. T. May, J. Haynes, C. Jakob, E. O'Connor, M. Pope, and M. C. Wheeler, 2011: The variability of tropical ice cloud properties as a function of the large-scale context from ground-based radar-lidar observations over Darwin, Australia. Atmos. Chem. Phys., **11**, 8363–8384.

Rutledge, S. A., E. R. Williams, and T. D. Keenan, 1992: The down upper Doppler and electricity experiment (DUNDEE): Overview and preliminary results. Bull. Amer. Meteor. Soc., **73,** 3–16.

Simpson, J., T. D. Keenan, B. Ferrier, R. H. Simpson, and G. J. Holland, 1993: Cumulus mergers in the maritime continent. Meteor. Atmos. Phys., **51,** 73–99.

Steiner, M., and R. A. Houze Jr., and S. E. Yuter, 1995: Climatological characterization of three-dimensional storm structure from operational radar and rain gauge data. J. Appl. Meteor., **34,** 1978–2007.

Westcott, N. E. 1994: Merging of convective clouds: cloud initiation, bridging, and subsequent growth. Mon. Wea. Rev., **122**, 780-790.

Williams, E. R., S. A. Rutledge, S. G. Geotis, N. Renno, E. Rasmussen, and T. Rickenbach, 1992: A radar and electrical study of tropical hot towers. J. Atmos. Sci., **49,** 1386–1395.

van den Broeke, M. S., D. M. Schultz, R. H. Johns, J. S. Evans, J. E. Hales, 2005: Cloud-to-ground lightning production in strongly forced, low-instability convective lines associated with damaging wind. Wea. Forecasting, **20**, 517–530.

Table 1: Distribution of the large-scale atmospheric regimes, convective cloud activity and associated lightning strokes in our two-season sample. The data ranges represent the 95% confidence intervals.

Regime	Total Days [Oct, Nov, Dec, Jan Feb, Mar, Apr]	Steiner Pixels		TITAN Cells with lifetime > 10 mins				
		Counts Per day	Lightning flashes per minute per pixel	Counts per day	Lightning flashes per minute per cell	Lifetime (mins)	Speed (m s^{-1})	Volume (km^3)
Dry East (DE)	38 [18, 11, 4, 0, 2, 0, 3]	156– 407	0.11 – 0.19	2 – 6	20.2 – 28.7	40.2 – 52.4	6.6 – 8.7	76 – 129
East (E)	25 [0, 7, 8, 0, 0, 0, 10]	1210 – 1861	0.12 – 0.17	20 – 35	15.2 – 18. 2	41.3 – 47.23	3.6 – 4.4	84 – 120
Deep West (DW)	64 [1, 2, 3, 27, 1, 28, 2]	11076 – 11827	0.008 – 0.010	91 – 100	0.9 – 1.3	38.8 – 40.4	5.89 – 7.5	61–75
Shallow West (SW)	59 [0, 12, 4, 16, 18, 5, 4]	7957 – 8390	0.07 – 0.09	54 – 67	10.4 – 11.1	42.1 – 44.8	5.0 – 6.0	87 – 107
Moist East (ME)	175 [0, 19, 43, 19, 35, 29, 30]	7261 – 7896	0.06 – 0.07	60 – 70	8.2 – 9.1	43.5 – 45.1	4.5 – 5.0	93 – 105

Figure Captions:

Fig. 1: Sampling domain of the Darwin C-band polarimetric radar (CPOL). The concentric rings in this figure and all subsequent figures are 50 km apart. Only data from the shaded gray region, i.e. ranges 20 – 120 km, are analysed in this paper. To better quantify the effects of the underlying surface type, the data for Fig. 12 are separated into oceanic (blue, ~2380 km^2), coastal (yellow, ~4160 km^2) and continental sectors (red, ~7280 km^2).

Fig. 2: Two-year mean profile of radiosonde measurements of (a) horizontal winds at 0.5 km vertical resolution, (b) corresponding vertical wind shear and (c) relative humidity, for the five large-scale atmospheric regimes (yellow: dry east (DE); black: east (E); blue: deep west (DW); green: shallow west (SW); red: moist east (ME)). The length of vectors in (a) and (b) corresponds to magnitude of the vectors; the scale is given on the top right hand corners. The North direction points upward in these figures.

Fig. 3: (a) Probability distribution function (PDF) of the maximum height of 5-dBZ echoes (ETH) for the respective large-scale atmospheric regimes using bin sizes of 1.0 km in height. (b) The lightning occurrence rate (strokes per number of convective pixels in each height bin) as a function of large-scale atmospheric regimes. The lightning flash occurrence varies significantly with increasing ETH, so a log scale has been used in Fig. 3b. The gray-shaded region in both figures represents the PDF obtained using data from all regimes, including the dry east regime.

Fig. 4: Spatial maps showing the mean height of the 5-dBZ echoes (top panels), the occurrence counts of convective pixels (middle panels), and occurrence count of

lightning strokes associated with these convective pixels (bottom panels) for the respective large-scale atmospheric regimes. A bin size of 5 km x 5 km is used here with maximum coverage of 120 km from the radar centre. The occurrence counts in second panels are expressed as a fraction of maximum possible number of measurements per bin.

Fig. 5: The same format as Fig. 3a and shows PDF of TITAN (a) cell lifetime using bin size of 10 min in time (b) and cell speed using bin size of 1 m s^{-1} for the respective large-scale atmospheric regimes. As discussed in the text, only TITAN cells with lifetime greater 10 min (and cells that formed and decayed within 140 km of the radar centre) is in used in this figure and all subsequent figures.

Fig. 6: Spatial maps of total number of TITAN tracks per day in 20 km x 20 km bins (top panels), percentage of TITAN cells rejected by our filters (cells within 140 km vs all cells with lifetime greater 10 min; second panels), their average displacement using a feather plot (third panels), average lifetime (fourth panels) and average speed (five panels) for the respective large-scale atmospheric regimes. Spatial bins with missing vector or white colour indicates that bin contained fewer than five TITAN tracks. The length of vectors in the third panels represents the mean ground displacement of the cells.

Fig. 7: The same format as Fig. 3a and shows PDF of TITAN cell volume using bin size of 20 km^3.

Fig. 8: The same format as Fig. 6 except shows the spatial maps of average cell volume per 20 km x 20 km bins.

Fig. 9: The same format as Fig. 3a and shows PDF of the TITAN cell onset times using bin size of 1 hr in local time.

Fig. 10: The same format as Fig. 6 except shows the spatial maps of the dominant local time period at the onset of TITAN cells per 20 km x 20 km bins.

Fig. 11: The time-height distribution of the frequency of occurrence of 5-dBZ echoes at the top of convective clouds identified using the Steiner classification for the E (top panel), DW (second panel), SW (third panel) and ME (bottom panel). A bin size of 1-hr in local time and 1-km in height is used in these plots. The echo counts per bin are firstly divided by total number of days of respective regime, and then expressed as a percentage of the highest bin echo count per panel. The highest count is stated on the bottom right hand corner in each panel. The black curves are the mean diurnal variation of 5-dBZ cloud height with the solid curve for each regime and the black-while dashed curve calculated using data from all regimes, including the dry east regime. The solid white curve is total lightning counts.

Fig. 12: The time-height distribution of the frequency of occurrence of 5-dBZ echoes above convective clouds identified using Steiner classification for the (a) DW and (b) ME regimes. The top panels show all echoes, second panels are for echoes located above the oceanic region, third panels for coastal region and bottom panels for continental regions. All panels are in the same format as Fig. 11, except count has been normalised by respective area of each underlying surface type. The three underlying surface types are highlighted in Fig. 1

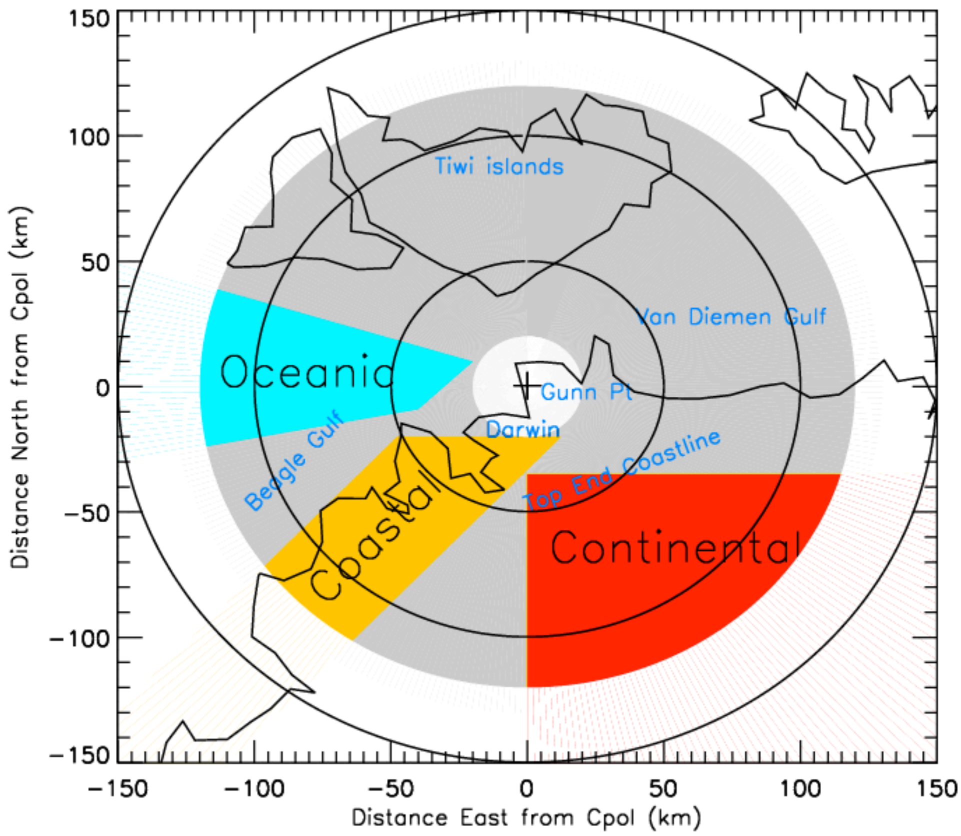

Fig. 1: Sampling domain of the Darwin C-band polarimetric radar (CPOL). The concentric rings in this figure and all subsequent figures are 50 km apart. Only data from the shaded gray region, i.e. ranges 20 – 120 km, are analysed in this paper. To better quantify the effects of the underlying surface type, the data for Fig. 12 are separated into oceanic (blue, ~2380 km^2), coastal (yellow, ~4160 km^2) and continental sectors (red, ~7280 km^2).

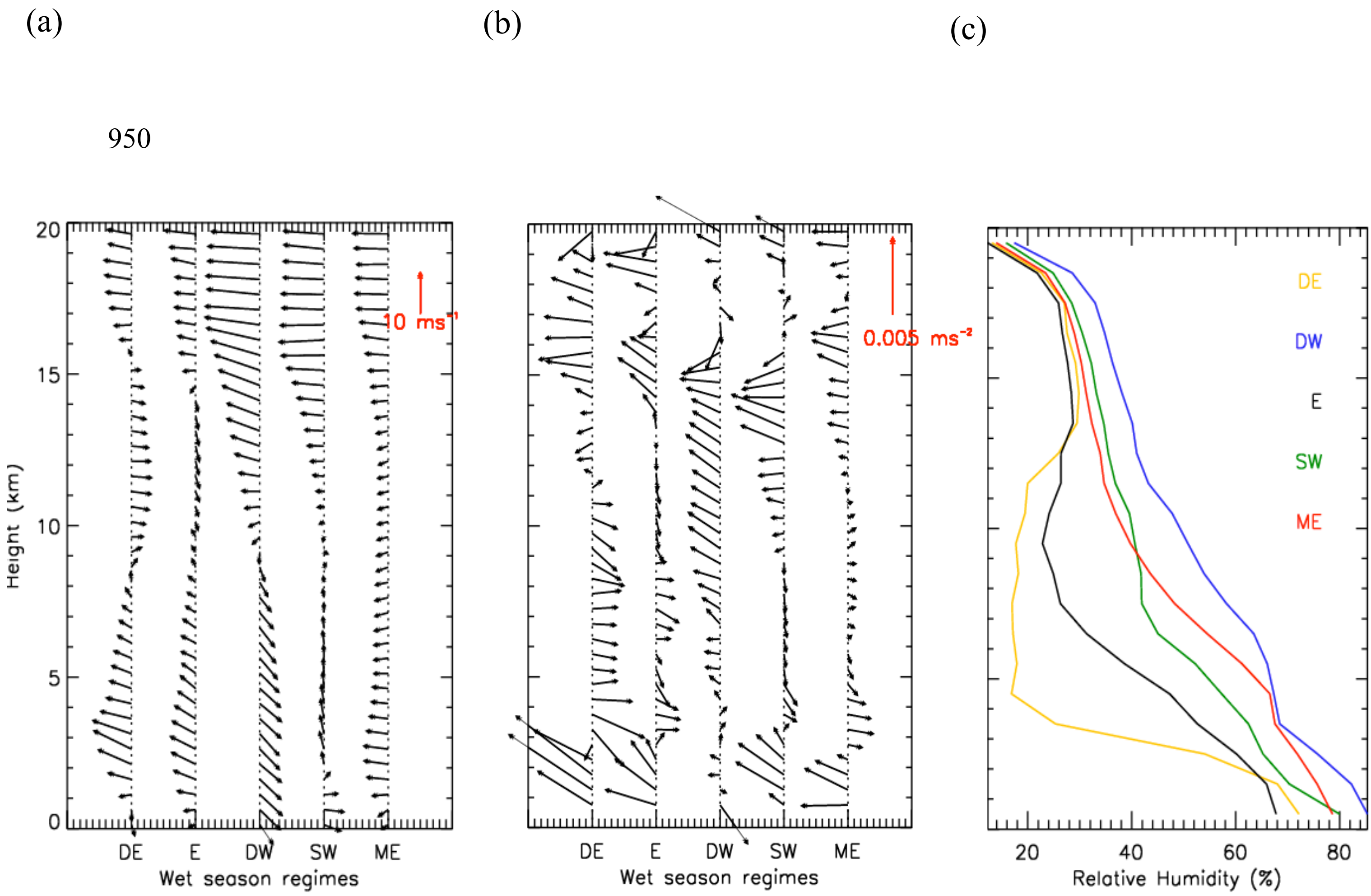

Fig. 2: Two-year mean profile of radiosonde measurements of (a) horizontal winds at 0.5 km vertical resolution, (b) corresponding vertical wind shear and (c) relative humidity, for the five large-scale atmospheric regimes (yellow: dry east (DE); black: east (E); blue: deep west (DW); green: shallow west (SW); red: moist east (ME)). The length of vectors in (a) and (b) corresponds to magnitude of the vectors; the scale is given on the top right hand corners. The North direction points upward in these figures.

(a) (b)

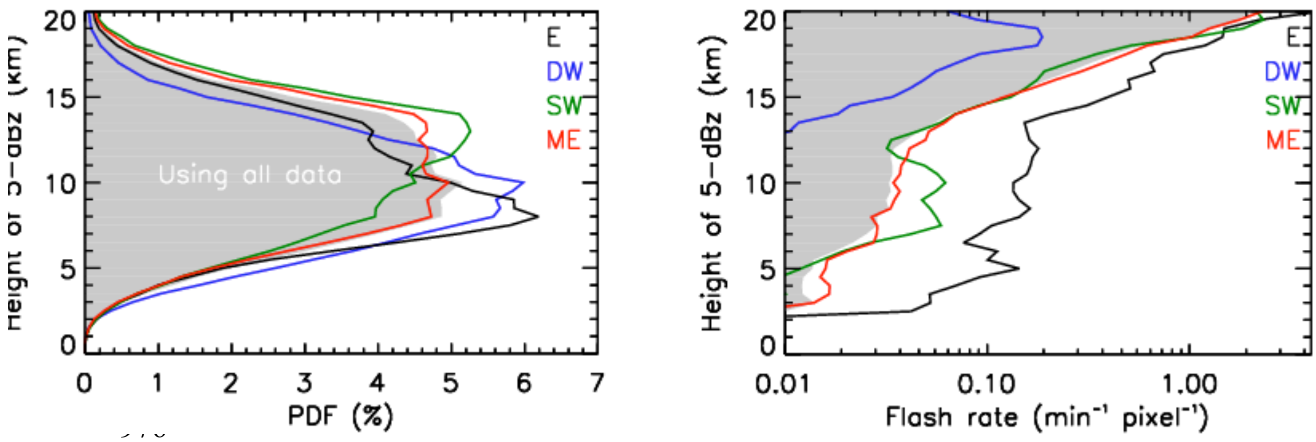

Fig. 3: (a) Probability distribution function (PDF) of the maximum height of 5-dBZ echoes (ETH) for the respective large-scale atmospheric regimes using bin sizes of 1.0 km in height. (b) The lightning occurrence rate (strokes per number of convective pixels in each height bin) as a function of large-scale atmospheric regimes. The lightning flash occurrence varies significantly with increasing ETH, so a log scale has been used in Fig. 3b. The gray-shaded region in both figures represents the PDF obtained using data from all regimes, including the dry east regime.

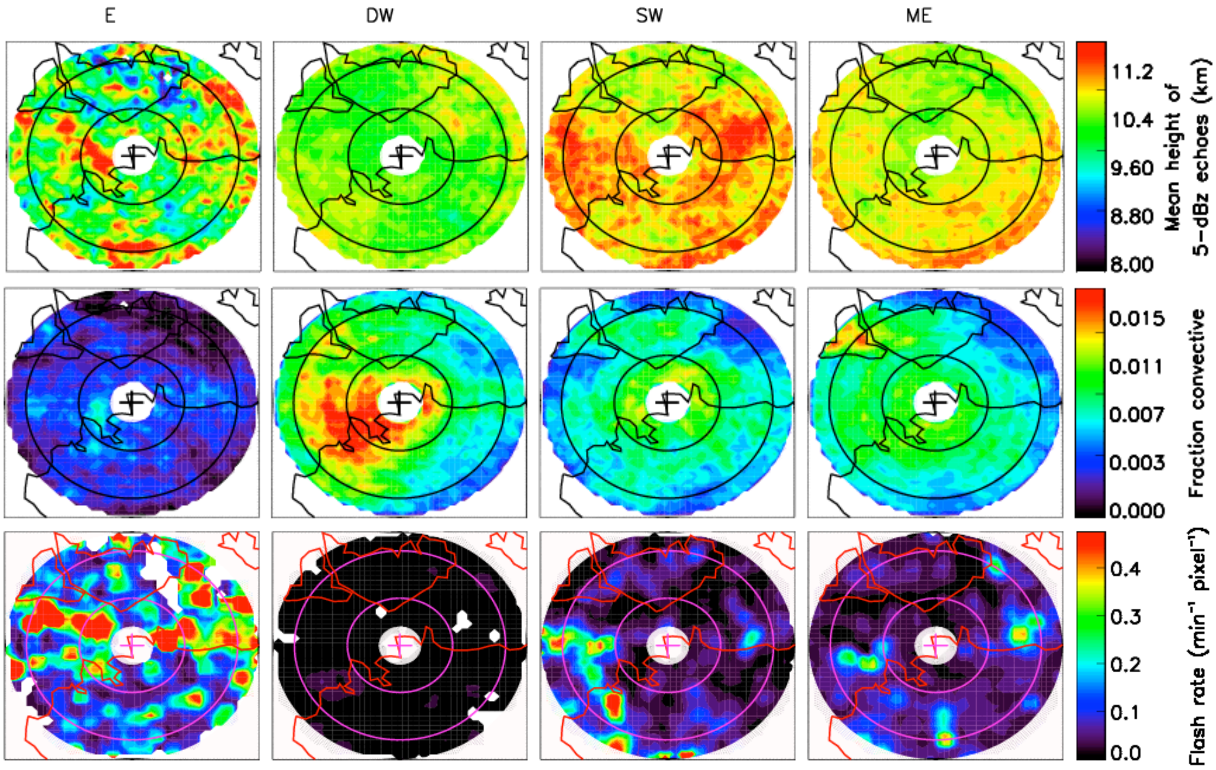

Fig. 4: Spatial maps showing the mean height of the 5-dBZ echoes (top panels), the occurrence counts of convective pixels (middle panels), and occurrence count of lightning strokes associated with these convective pixels (bottom panels) for the respective large-scale atmospheric regimes. A bin size of 5 km x 5 km is used here with maximum coverage of 120 km from the radar centre. The occurrence counts in second panels are expressed as a fraction of maximum possible number of measurements per bin.

(a)

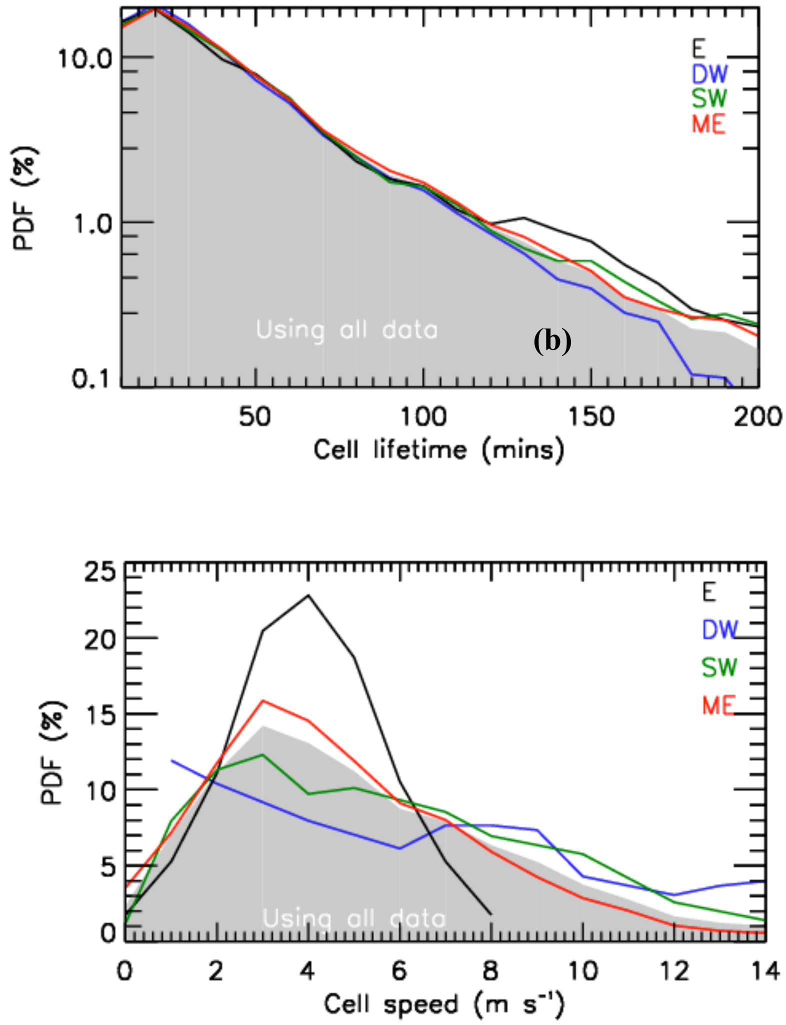

Fig. 5: The same format as Fig. 3a and shows PDF of TITAN (a) cell lifetime using bin size of 10 min in time (b) and cell speed using bin size of 1 m s^{-1} for the respective large-scale atmospheric regimes. As discussed in the text, only TITAN cells with lifetime greater 10 min (and cells that formed and decayed within 140 km of the radar centre) is in used in this figure and all subsequent figures.

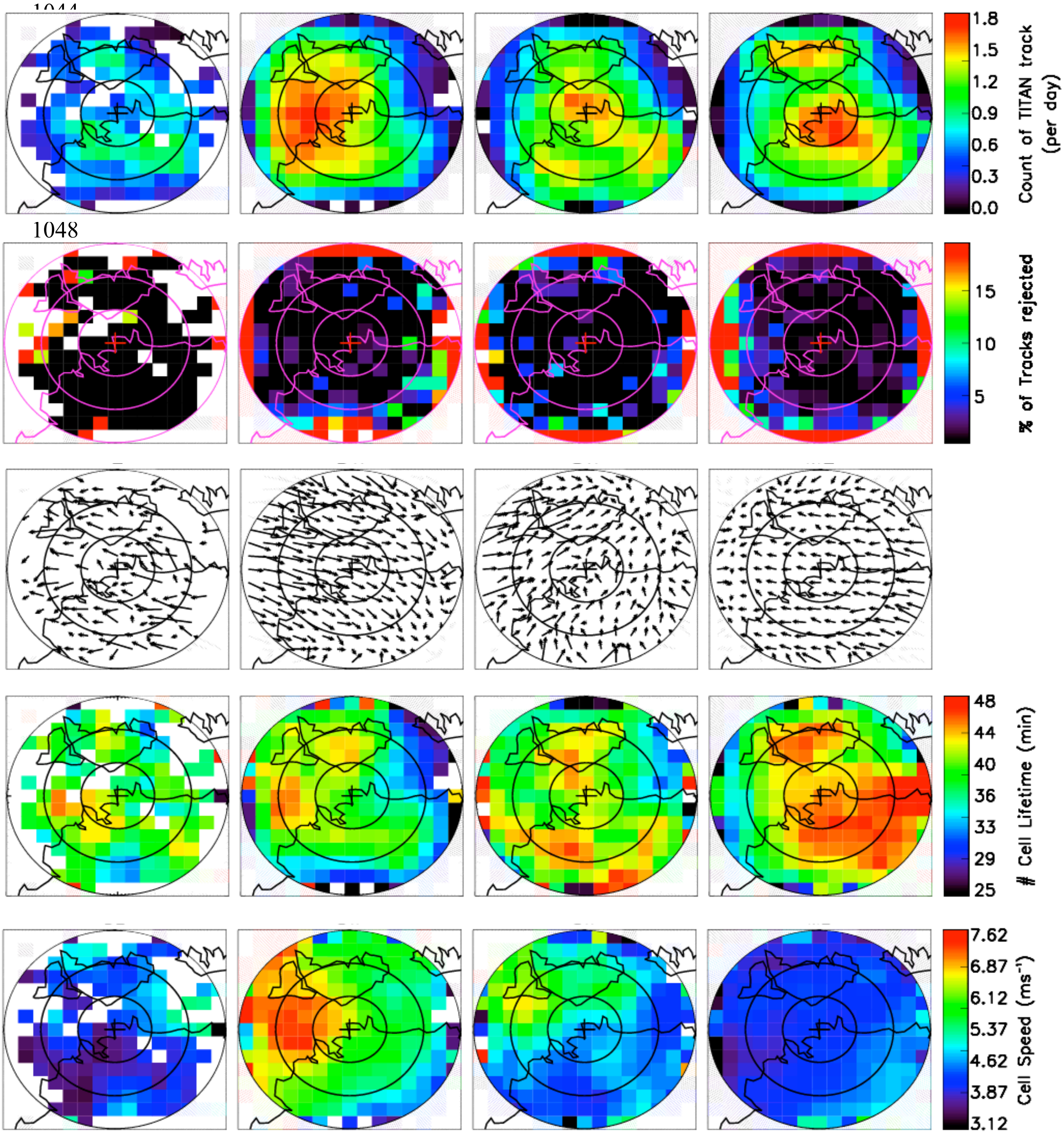

Fig. 6: Spatial maps of total number of TITAN tracks per day in 20 km x 20 km bins (top panels), percentage of TITAN cells rejected by our filters (cells within 140

km vs all cells with lifetime greater 10 min; second panels), their average displacement using a feather plot (third panels), average lifetime (fourth panels) and average speed (five panels) for the respective large-scale atmospheric regimes. Spatial bins with missing vector or white colour indicates that bin contained fewer than five TITAN tracks. The length of vectors in the third panels represents the mean ground displacement of the cells.

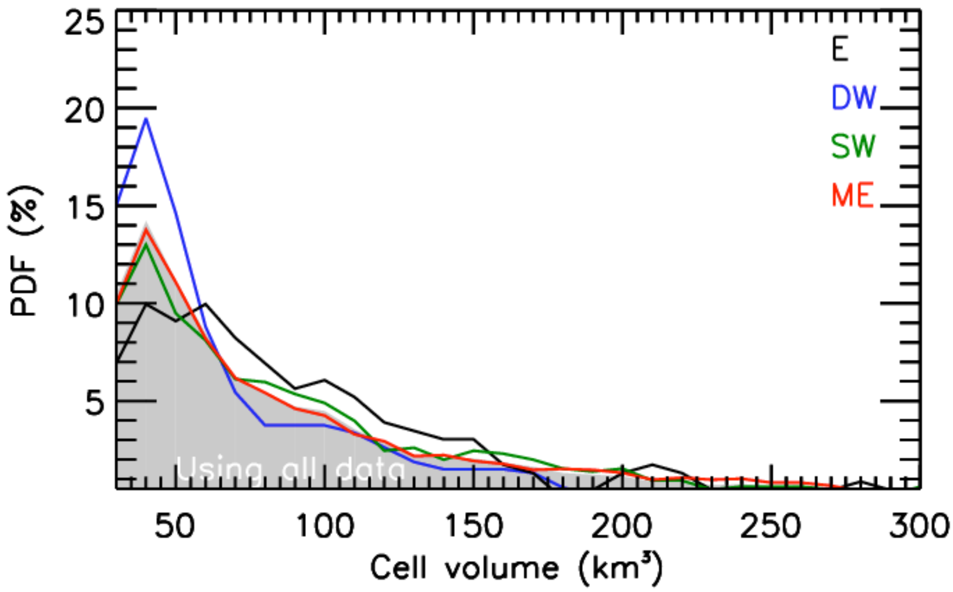

Fig. 7: The same format as Fig. 3a and shows PDF of TITAN cell volume using bin size of 20 km^3.

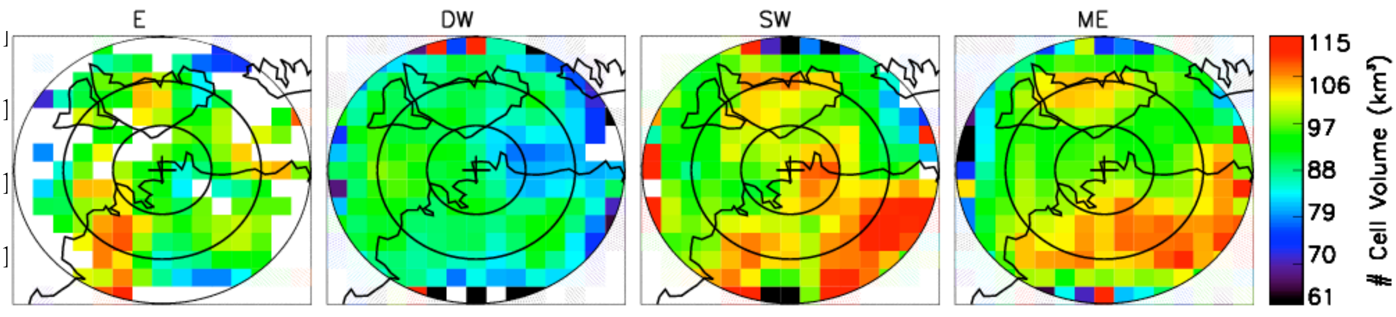

Fig. 8: The same format as Fig. 6 except shows the spatial maps of average cell volume per 20 km x 20 km bins.

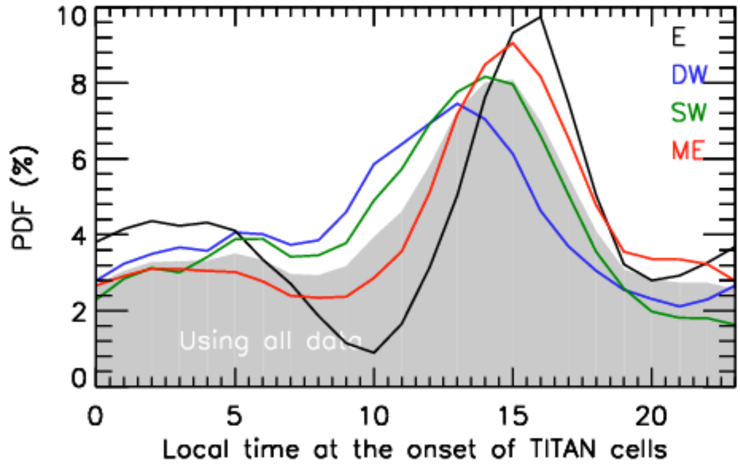

Fig. 9: The same format as Fig. 3a and shows PDF of the TITAN cell onset times using bin size of 1 hr in local time.

DW **SW** **ME**

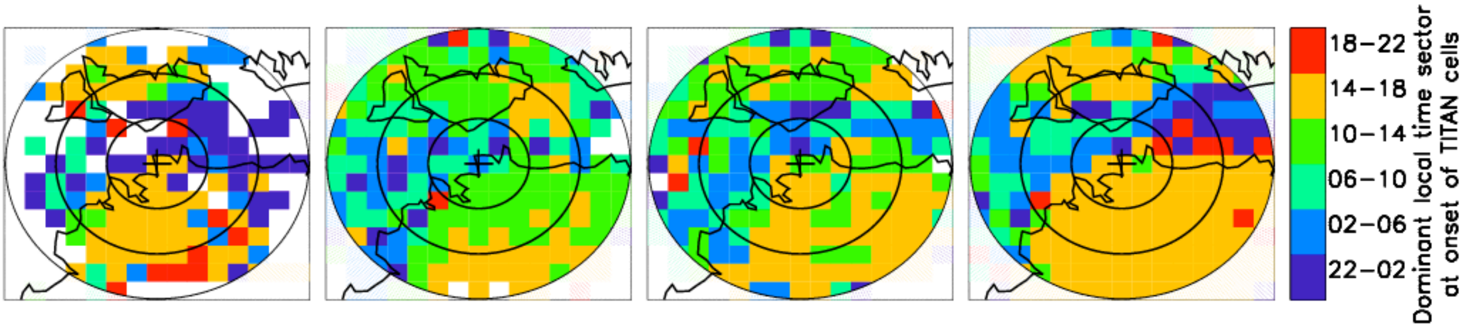

Fig. 10: The same format as Fig. 6 except shows the spatial maps of the dominant local time period at the onset of TITAN cells per 20 km x 20 km bins.

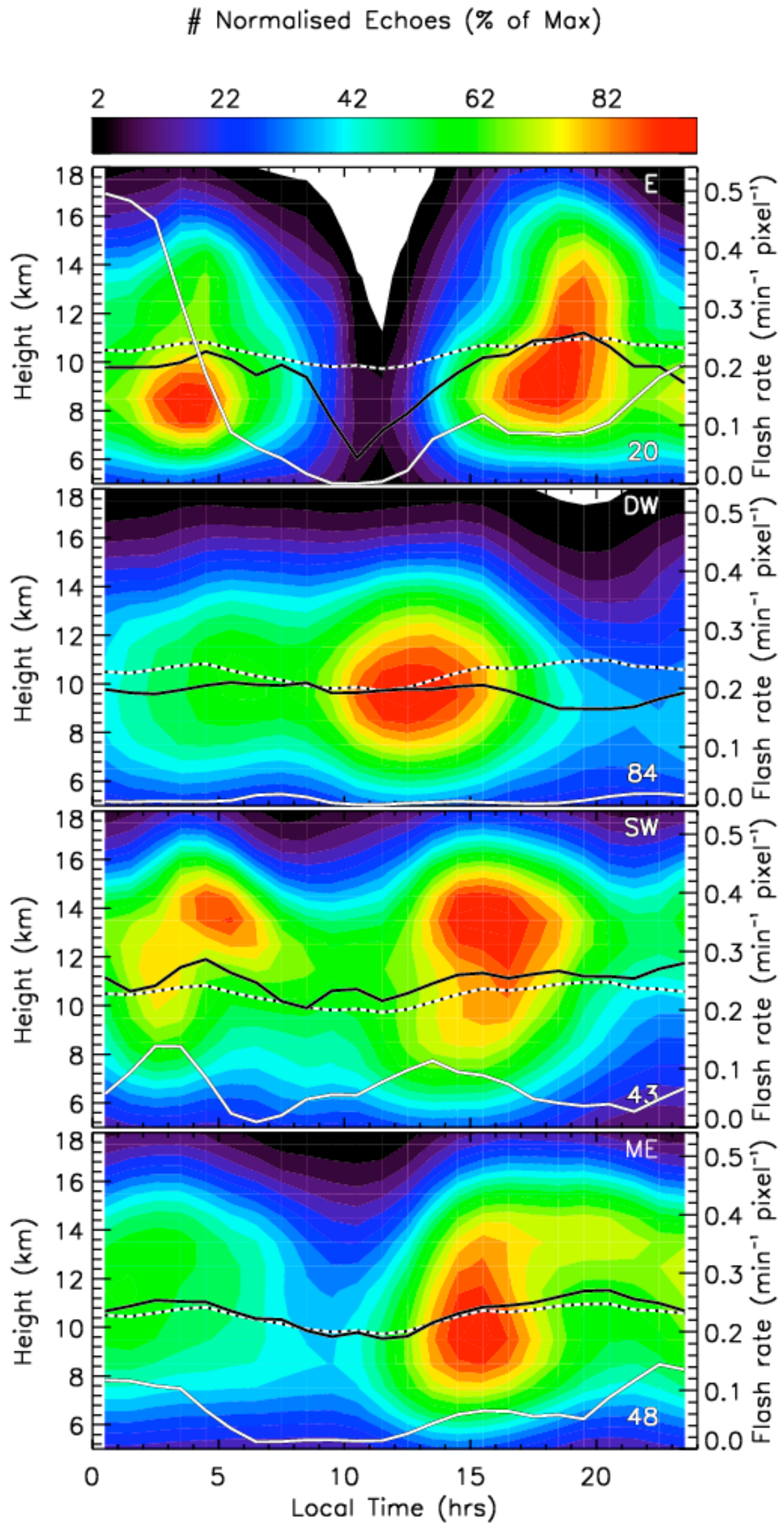

Fig. 11: The time-height distribution of the frequency of occurrence of 5-dBZ echoes at the top of convective clouds identified using the Steiner classification for the E (top panel), DW (second panel), SW (third panel) and ME (bottom panel). A bin size of 1-hr in local time and 1-km in height is used in these plots. The echo counts

per bin are firstly divided by total number of days of respective regime, and then expressed as a percentage of the highest bin echo count per panel. The highest count is stated on the bottom right hand corner in each panel. The black curves are the mean diurnal variation of 5-dBZ cloud height with the solid curve for each regime and the black-while dashed curve calculated using data from all regimes, including the dry east regime. The solid white curve is total lightning counts.

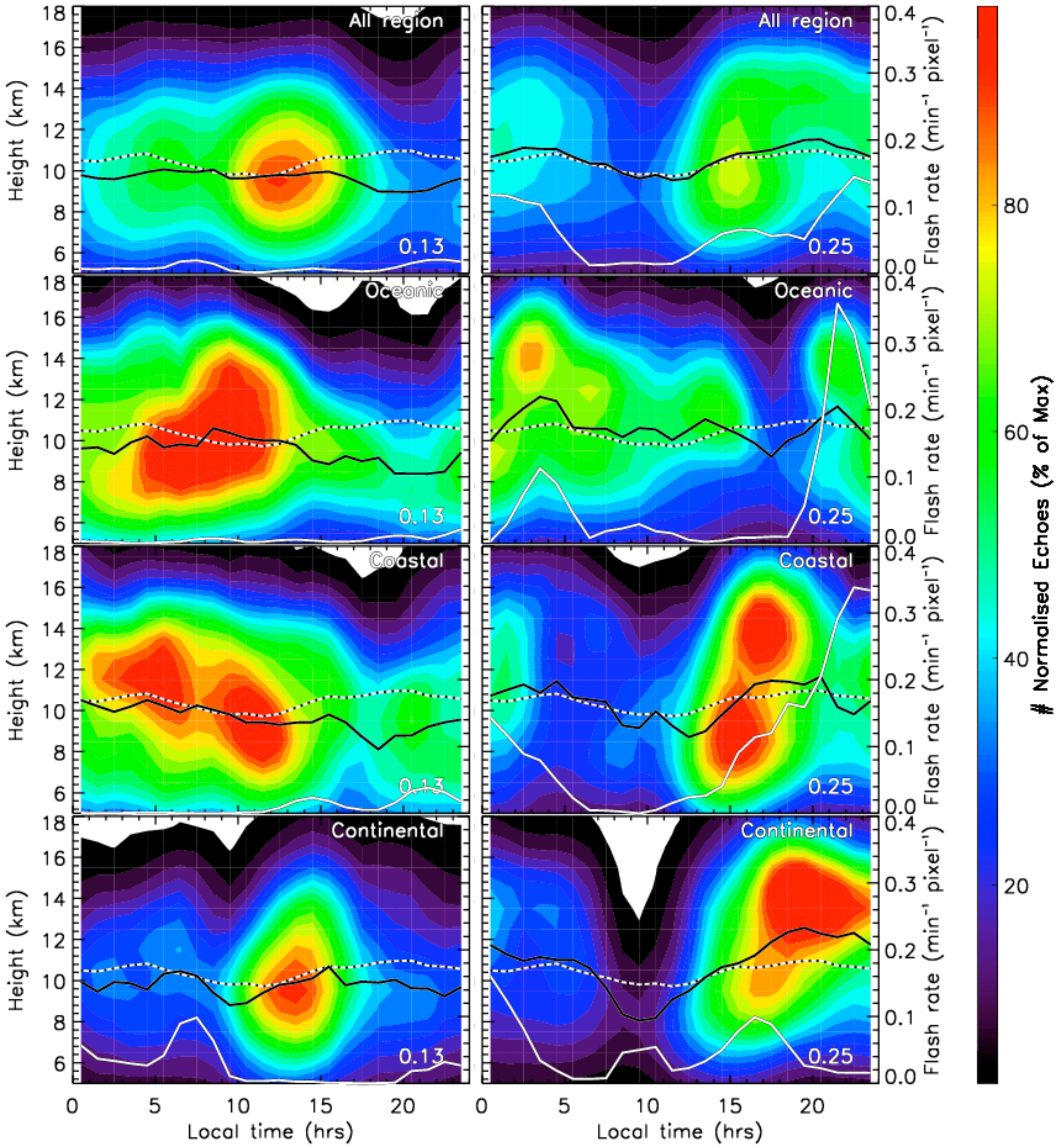

Fig. 12: The time-height distribution of the frequency of occurrence of 5-dBZ echoes above convective clouds identified using Steiner classification for the (a) DW and (b) ME regimes. The top panels show all echoes, second panels are for echoes located above the oceanic region, third panels for coastal region and bottom panels for continental regions. All panels are in the same format as Fig. 11, except count has been normalised by respective area of each underlying surface type. The three underlying surface types are highlighted in Fig. 1

1274